AIAA SciTech Forum
8-12 January 2024, Orlando, FL
AIAA SCITECH 2024 Forum

10.2514/6.2024-0495

Modal Decomposition of K-Type Boundary Layer Transition

Cong Lin* and Oliver T. Schmidt†
University of California San Diego, La Jolla, California 92093.

We perform a data-driven discovery of the physics within transition mechanisms by using a suite of modal decomposition techniques on the DNS of deterministic K-type boundary layer transition. Specifically, we deploy Spectral Proper Orthogonal Decomposition (SPOD) and Space-Time POD (STPOD) along with a D1 Symmetry Decomposition to educe coherent structures in time and frequency domain, with different optimality properties each, and establish their relationships to each other. Our study is in part a data-driven counterpart to a recent harmonic balancing study by Rigas et al. [1]: Therein we verify which pre-turbulence transition mechanisms are reproducible by a varying number of Fourier-type modes at the fundamental frequency and its harmonics. In extension, we identify from data the prototypical transition scenario, extract modes associated with various instability mechanisms and uncover how far these distinct coherent structures persevere into the developed turbulence. We investigate energetic exchanges in the transitional and turbulent regimes with particular emphasis on the emergence of periodic and non-periodic, as well as symmetric and anti-symmetric structures within the flow.

I. Introduction and Overview

Boundary layer transition caused by deterministic input actuation has been the subject of extensive study over the last few decades. In the seminal study from 1995, Rist and Fasel [2] conducted direct numerical simulations (DNS) of controlled K-type transition in a flat-plate boundary layer, successfully reproducing wind tunnel experiments by Kachanov et al. [3, 4] and providing valuable insights into structures within the fundamental breakdown process. Bake et al. [5] (2002) laid the foundational groundwork for studying the complex flow randomization process that transforms the deterministic actuation into developed boundary layer turbulence through amplification of disturbances from the background and freestream. Sayadi et al. [6] (2013) conducted comprehensive studies of complete K- and H-type transitions, demonstrating their convergence towards fully developed turbulence after the skin-friction overshoot and revealing that a periodic hairpin-packet solution in the late stages of transition yields statistical properties resembling developed turbulence. Most recently, Rigas et al. [1] (2021) extended linear input/output (resolvent) analysis to account for nonlinear triadic interactions via a harmonic balance model with a minimal frequency-wavenumber basis, enabling the identification of worst-case finite-amplitude disturbances that maximize drag and solving various transition scenarios up to the skin friction maximum directly within the frequency domain. In our study, we aim to expand our understanding of the physical mechanisms further into turbulence by using statistical modal analysis techniques with particular emphasis on harmonic analysis, non-periodic spatio-temporal dynamics and symmetry breaking.

After re-creating the controlled K-type transition scenario and validating it against the literature [2, 6], we use a D1 symmetry decomposition to reveal how much of the transition mechanisms of interest can be captured in the symmetric versus the anti-symmetric components. We compare our data-driven analysis to the Harmonic Balance approach in Rigas et al. [1] by reproducing significant pre-turbulence transition mechanisms using a small range of SPOD modes at the fundamental frequency and its harmonics. In extension, we also demonstrate the precise linear combinations of SPOD modes needed to reconstruct a hairpin vortex solution and subsequently the complete dominant harmonic transition mechanism under a harmonic basis assumption. Finally, we extend our analysis beyond the skin-friction maximum with Space-Time POD to identify both periodic and non-periodic spatio-temporal structures. As the flow dynamics evolve from periodic to quasi-periodic and eventually to chaotic/turbulent with asymmetry, we present the modes that identify the specific streamwise locations where the transitions between these different dynamical states occur. Simultaneously, we shed light on the energetic transfer between all of these modes as the analysis progresses from upstream to downstream. Our analysis thus provides further advances and insights in understanding the intricate progression from controlled, deterministic transitional flow to fully developed boundary layer turbulence.

---

*Graduate Student Researcher, Mechanical and Aerospace Engineering. Student Member AIAA.

†Associate Professor, Mechanical and Aerospace Engineering. Senior Member AIAA

II. Methods: Data and Modal Decomposition Techniques

In this section, we present the methodology for the three decomposition techniques used in our study to compute modes from the spatio-temporal flow field of interest $\mathbf{q}(\mathbf{x}, t)$. We start from the most general to most specialized: D1 symmetry decomposition, Space-Time Proper Orthogonal Decomposition (STPOD), Spectral Proper Orthogonal Decomposition (SPOD).

A. Symmetry Decomposition (D1)

The symmetric component of the flow field is defined as

$$\mathbf{q}_S(x, y, z) = \frac{1}{2}\begin{bmatrix} u(x, y, z) + u(x, y, -z) \\ v(x, y, z) + v(x, y, -z) \\ w(x, y, z) - w(x, y, -z) \end{bmatrix} \tag{1}$$

while the anti-symmetric component is given by

$$\mathbf{q}_A(x, y, z) = \frac{1}{2}\begin{bmatrix} u(x, y, z) - u(x, y, -z) \\ v(x, y, z) - v(x, y, -z) \\ w(x, y, z) + w(x, y, -z) \end{bmatrix}. \tag{2}$$

In our analysis, we leverage the natural transverse D1 (Dihedral group 1) symmetry stemming from the simulation setup and the symmetry of the actuation. While not conventionally termed a *modal* decomposition method, a symmetry decomposition can be applied to the DNS data before each modal decomposition method − the additivity and linearity properties allow for its application without a loss of generality. As recommended by Sirovich [7], this ensures the expected statistical symmetries of resulting modes, generating either symmetric or anti-symmetric modes without modes that are a mixture of both. Furthermore, this approach effectively cuts the computational and memory requirements in half, as the modal decompositions can then be separately applied to the symmetric and anti-symmetric components one at a time. Physically, this method also provides additional insights into the downstream mechanisms and statistics of symmetry breaking in the present flow system.

B. Space-Time Proper Orthogonal Decomposition (STPOD)

The space and finite-time POD problem, first formulated by Lumley [8] and recently computed by Schmidt and Schmid [9] with a conditional formulation for finite events of interest, can be solved via the following Fredholm eigenvalue problem

$$\int_{\Delta T}\int_{V} E\{\mathbf{q}(\mathbf{x}, t)\mathbf{q}^*(\mathbf{x}', t')\}\boldsymbol{W}(\mathbf{x})\boldsymbol{\phi}(\mathbf{x}, t)\, d\mathbf{x}'\, dt' = \lambda\boldsymbol{\phi}(\mathbf{x}, t), \tag{3}$$

defined over a specific finite time interval ΔT. Here, $(\cdot)^*$ denotes the complex conjugate, V the spatial domain, and $\boldsymbol{W}(\mathbf{x})$ is a positive definite spatial weight matrix. This yields the space-time POD modes given by $\boldsymbol{\phi}(\mathbf{x}, t)$ that are orthogonal in the space-time inner product

$$\langle \mathbf{q}_1, \mathbf{q}_2 \rangle_{\mathbf{x},\Delta T} = \int_{\Delta T}\int_{V} \mathbf{q}_1^*(\mathbf{x}, t)\boldsymbol{W}(\mathbf{x})\mathbf{q}_2(\mathbf{x}, t) dV dt \tag{4}$$

and respective eigenvalues λ that maximizes

$$\lambda = \frac{E\{|\langle \mathbf{q}(\mathbf{x}, t), \boldsymbol{\phi}(\mathbf{x}, t)\rangle_{\mathbf{x},\Delta T}|^2\}}{\langle \boldsymbol{\phi}(\mathbf{x}, t), \boldsymbol{\phi}(\mathbf{x}, t)\rangle_{\mathbf{x},\Delta T}}. \tag{5}$$

Here, $E\{\mathbf{q}(\mathbf{x}, t)\mathbf{q}^*(\mathbf{x}', t')\} = \boldsymbol{C}(\mathbf{x}, \mathbf{x}', t, t')$ is the statistical estimate of the two-point space–time correlation tensor, where $\mathbf{q}(\mathbf{x}, t)$ is sampled with respect to the event of interest H. Thus, in its discrete space and time equivalent the STPOD problem can be realized by the eigen-decomposition

$$\mathbf{Q}\mathbf{Q}^*\mathbf{W}\boldsymbol{\Phi} = \boldsymbol{\Phi}\boldsymbol{\Lambda} \tag{6}$$

where, for each realization of the event H, the snapshots of $\mathbf{q}(\mathbf{x},t)$ are stacked vertically on each other over the finite time window ΔT in the column space of $\mathbf{Q}$ and different realizations are then concatenated in row-order. For further details of the algorithm we refer to [9, 10]. The space-time POD modes are then coherent structures, orthogonal by construction in space and over finite time ΔT, with their evolution recovered in the columns of $\mathbf{\Phi}$ each and their eigenvalues (i.e. energies) recovered in $\mathbf{\Lambda}$. In the context of this work, ΔT spans the length of one period. We remark that STPOD is the most general method here that makes the least restrictive assumptions about the space-time signal $\mathbf{q}(\mathbf{x},t)$.

There are two notable limit cases for STPOD, as recently generalized by Frame and Towne [10]: In the limit of $\Delta T \to 0$, we recover the popular "space-only" POD or "snapshot" POD (Sirovich [11], Aubry [12]). In the formal limit of $\Delta T \to [-\infty,\infty]$ and assuming statistical stationarity, the STPOD problem becomes SPOD, which we will briefly introduce in the following.

C. Spectral Proper Orthogonal Decomposition (SPOD)

Spectral Proper Orthogonal Decomposition (SPOD) [13], is the frequency domain version of POD and derivable from the STPOD problem in the limit of $\Delta T \to [-\infty,\infty]$ assuming statistical stationarity. Under that condition, the space-time correlation tensor depends only on the difference $\tau = t - t'$ between two times, i.e., $\boldsymbol{C}(\mathbf{x},\mathbf{x}',t,t') \to \boldsymbol{C}(\mathbf{x},\mathbf{x}',\tau)$, which allows the definition of the cross-spectral density tensor via the Fourier transform of the two-point space-time correlation tensor:

$$\boldsymbol{S}(\mathbf{x},\mathbf{x}',f) = \int_{-\infty}^{\infty} \boldsymbol{C}(\mathbf{x},\mathbf{x}',\tau)e^{-2\pi i f\tau}d\tau = E\{\hat{\mathbf{q}}(\mathbf{x},f)\hat{\mathbf{q}}^*(\mathbf{x}',f)\} \tag{7}$$

where $\hat{\mathbf{q}}$ is the temporal Fourier transform of $\mathbf{q}$. Thus, instead of solving the Fredholm eigenvalue problem of Eq. (3) with infinite time integration bounds, one can solve the Fourier-transformed eigenvalue problem

$$\int_V E\{\hat{\mathbf{q}}(\mathbf{x},f)\hat{\mathbf{q}}^*(\mathbf{x}',f)\}\boldsymbol{W}(\mathbf{x})\boldsymbol{\psi}(\mathbf{x}',f)\,d\mathbf{x}' = \lambda(f)\boldsymbol{\psi}(\mathbf{x},f), \tag{8}$$

as a spatial eigenvalue problem in the frequency domain for each frequency f. Thus, the discrete equivalent is realized as

$$\hat{\mathbf{Q}}_{f_k}\hat{\mathbf{Q}}^*_{f_k}\mathbf{W}\mathbf{\Psi}_{f_k} = \mathbf{\Psi}_{f_k}\mathbf{\Lambda}_{f_k}, \tag{9}$$

with $\hat{\mathbf{Q}}_{f_k}$ denoting the Fourier realizations matrix at each discrete frequency f_k, that stores different realizations of the Fourier modes $\hat{\mathbf{q}}(\mathbf{x}, f_k)$ as the flow evolves. For further details on the SPOD algorithm we refer to [14]. The eigenvectors $\mathbf{\Psi}_{f_k}$ are the SPOD modes ranked in column-order at frequency f_k and the eigenvalues $\mathbf{\Lambda}_{f_k}$ are the corresponding modal energies of each mode. Algorithmically, SPOD uses Welch's method [15] to estimate the spectral densities.

SPOD modes are single-frequency coherent structures that are orthogonal in space-time indefinitely and optimally capture the variance of the data at that frequency. They can thus be viewed as optimal Fourier modes and are formally equivalent to resolvent modes in the case of white noise forcing as shown by Towne et al. [14].

III. Direct Numerical Simulation and Validation of K-type Transition

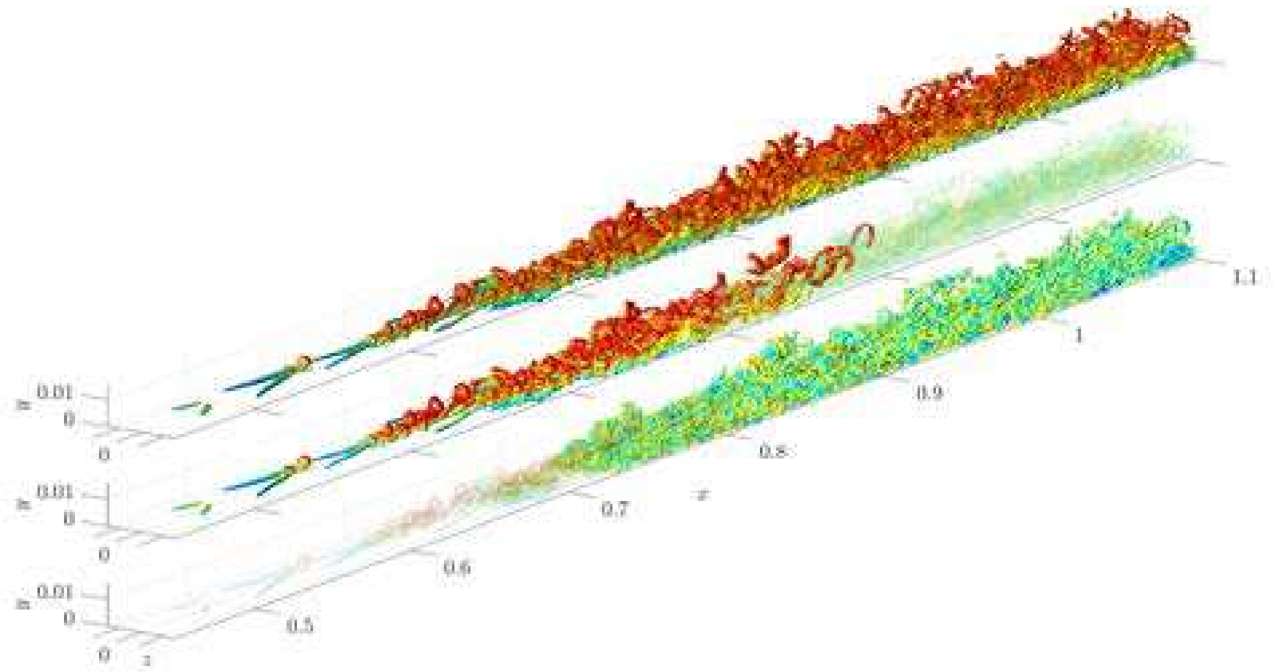

Fig. 1 Regimes of the transition process − deterministic to turbulent. Top: instantaneous DNS snapshot; middle: fundamental STPOD mode ϕ_0 (periodic phase mean $\tilde{q}$); bottom: cyclo-stationary component q''. Q-criterion isosurfaces colored in the stream-wise velocities of the respective quantities ($Q = 10^3$), corresponding to $Re_x = 2.25 - 5.5 \times 10^5$.

A. Numerical Setup

Our numerical setup takes inspiration from previous studies by Sayadi et al. [6] and Fasel et al. [16] that computed K- and H-type transitions. The inlet Reynolds number (taken to be the non-dimensional reference length) from the leading edge is $Re_x = xU_\infty/\nu = 10^5$, where the kinematic viscosity is $\nu = 2 \times 10^{-6}$. We use a Mach number of $M = U_\infty/c_\infty = 0.2$ making this flow weakly compressible. The computational domain and resolution by Sayadi et al. [6] are used as a reference, however, we truncate the domain to minimize computational cost while retaining the required transition physics. With a dimensional reference length scale of $x_0 = 0.2$, our domain begins at one reference length scale from the leading edge (at $Re_x = 10^5$) and spans $1 < x/x_0 < 5.5$ in the streamwise, $0 < y/x_0 < 1$ in the wall-normal and $-0.075 < z/x_0 < 0.075$ in the spanwise direction. This allows us to fully capture one instability wave in the span, while excluding the region of pure fully developed turbulence onset from Sayadi et al. [6]. We opt to truncate the region of fully turbulent onset, as we are mainly interested in the region of transition to turbulence and based on results from [6], our domain extends sufficiently far into the turbulent section for all turbulence metrics to collapse to self-similarity.

Our DNS mesh consists of two regions, a finer wall region, and a coarser free stream region, each comprised of purely Cartesian cells with a single layer of polyhedral cells connecting them. We fully resolve the wall region ($0 < y/x_0 < 0.15$) such that the vertical height of the cells closest to the wall is $y^+ \equiv yu^*/\nu < 1$ in viscous wall units. The wall region mesh is resolved with $N_x = 5600$ and $N_z = 128$ cells uniformly in the streamwise and spanwise directions, respectively, and $N_y = 257$ cells in the wall-normal direction with a geometric refinement rate towards the wall to fully resolve the wall turbulence.

For the calculation of the DNS we use the compressible flow solver CharLES [17] in DNS mode without subgrid scale and wall models. At the domain inlet, the laminar boundary condition is derived from the compressible Blasius self-similar solution for $Re_x = 10^5$. Unlike the previous studies, our outflow condition is a non-reflecting Navier-Stokes Characteristics-based Boundary Condition (NSCBC), combined with a volumetric sponge that spans $5.0 < x/x_0 < 5.5$

to absorb any remaining acoustic reflections and ensure a smooth outflow. The far-field boundary follows the same types of boundary conditions as the outlet, with a sponge in the region $y/x_0 > 0.75$. The spanwise boundaries are periodic. Lastly, the wall has a no-slip and no-flow condition everywhere except at the disturbance strip that is located at $1.36 < x/x_0 < 1.56$. The deterministic harmonic excitation at this disturbance strip is given by

$$v(x, z, t) = A_a v_a(x) \sin(\omega_1 t) + A_s v_s(x) \cos(\beta z), \tag{10}$$

where $A_a = 5 \times 10^{-3}$ and $A_s = 1.3 \times 10^{-4}$ are constant factors. Concretely, the function consists of

$$\begin{aligned} v_a(x) &= \begin{cases} 15.1875\xi^5 - 35.4375\xi^4 + 20.25\xi^3, & \text{if } x_1 < x \leqslant x_m \\ -v_a(2x_m - x), & \text{if } x_m < x \leqslant x_2 \end{cases} \\ v_s(x) &= \begin{cases} -3\xi^4 + 4\xi^3, & \text{if } x_1 < x \leqslant x_m \\ v_s(2x_m - x), & \text{if } x_m < x \leqslant x_2, \end{cases} \end{aligned} \tag{11}$$

with $x_1 = 1.36x_0$, $x_2 = 1.56x_0$ and $x_m = (x_1 + x_2)/2$. Thus, there is a spanwise homogeneous part that features a fixed 5th-order polynomial shape function $v_a(x)$ modulated with a sinusoidal signal of fundamental frequency ω_1 in time and a spanwise oblique part that has fixed sinusoidal shape in z with wavenumber β and a 4th order polynomial $v_s(x)$ for weak steady inflow.

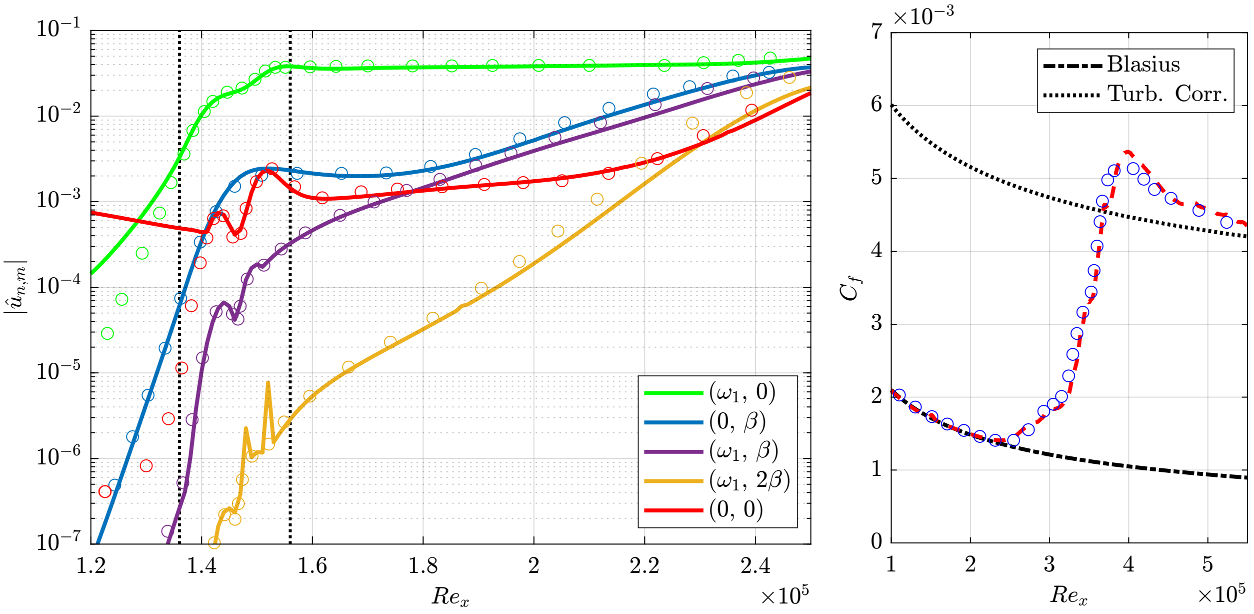

(a)

(b)

Fig. 2 DNS results and validation: a) stream-wise development of double Fourier mode $(n\omega_1, m\beta)$ amplitudes plotted against [2], vertical dotted lines indicate the extent of disturbance strip; b) C_f skin friction overshoot plotted against [6] ($C_f^{turb} = 0.455/\ln^2(0.06Re_x)$ correlation by [18]).

B. Post-excitation, Pre-transitional Dynamics

Fig.2a demonstrates a notable agreement with the literature [2]. The applied forcing creates initially planar modal Tollmien-Schlichting (TS) waves $(\omega_1, 0)$ and streaks $(0, \beta)$, at the given fundamental frequency and spanwise wavelength outlined in eq.(10). Nonlinear interactions then generate harmonics $(n\omega_1, m\beta)$ at integer multiples $n, m \in \mathbb{Z}$ of the fundamental frequency and wavelength as the flow develops. As perturbations progress in the streamwise direction, the streaks $(0, \beta)$, the oblique TS wave (ω_1, β), and the spanwise harmonic $(\omega_1, 2\beta)$ experience rapid amplification, driven by non-modal transient growth (lift-up mechanism) and other nonlinear interactions. The self-interaction of these higher modes, upon reaching high amplitudes, results in energy back-scattering to the mean-flow harmonic $(0, 0)$, leading to the departure of the mean flow from the Blasius base-flow and the growth of mean flow deformation. These mechanisms collectively lead to the formation of Λ-shaped vortices, which become streamwise elongated and lift away from the wall – eventually evolving into the characteristic hairpin vortices in the later stages of transition. The further streamwise flow development towards the skin friction ($C_f = 2\tau_w/U_\infty^2$) maximum is governed by the rise and amplitude growth of increasingly higher harmonics via a cascade of nonlinear interactions.

C. Transition to Skin-friction Overshoot and Onset of Turbulence

In Fig.2b, the streamwise development of skin friction coefficient (C_f) is found to be in good agreement with DNS data computed by Sayadi et al. [6], where we remark minor differences due to differences in the spanwise excitation function. Fig.2b and Fig.1 shows the departure of the C_f value from the laminar Blasius solution around $Re_x = 2.4 \times 10^5$ ($x = 0.48$), coinciding with the appearance of Λ vortices in that region. These Λ vortices are aligned in K-type transitions and get lifted away from the wall and progressively stretched out as they travel down the streamwise direction. They develop into hairpin vortices as their "heads" bulge further up into the freestream, transforming into Ω ring-like vortex heads via self-induction [5]. The instantaneous snapshot of our DNS data in Fig.1 (top) reveals these organized vortical structures in the transitional region that are characteristic for K-type transition, resembling results by Bake et al. [5], Sayadi et al. [6], Wu and Moin [19].

As analyzed by Bake et al. [5], the formation of Ω ring-like vortices at the tip of the Λ-vortices initiates an intricate flow randomization mechanism. In their initial stage, these vortices are highly sensitive to background perturbations while being accompanied by regions of very high induction and shear. These perturbed vortices strongly influence the surrounding fluid and particularly the adjacent wall region where this generates increasingly disturbed instantaneous pressure fields from one instance to the next. This in turn directly modifies the vorticity production at the wall for upcoming new instances. More downstream, the interaction of vortical structures from different disturbance periods leads to further amplification of background disturbances that generate new increasingly non-periodic, *chaotic* structures. With increasing randomization the eventual breakdown to chaos occurs with characteristics typical for a turbulent boundary layer.

In the later stages of transition, characterized by broken periodicity and increasing asymmetry, hairpin packets evolve into more convolved hairpin "forests", creating a self-sustaining auto-generation mechanism that reproduces the statistical properties of developed turbulence as shown by Sayadi et al. [6]. The distinct overshoot in the present K-type transition is observed that is absent in bypass transitions, e.g. Wu and Moin [20]. Fig. 2b indicates that after the skin-friction maximum occurs, C_f and the statistics asymptotically collapse onto the turbulent correlations, demonstrating good alignment with the literature and indicating the sufficient capture of the transitional region within our domain.

IV. Modal Decomposition Results

This analysis section follows a structured progression from upstream to downstream, employing methods tailored to analyze the local dynamics and statistics of each region. Given the initially periodic nature of the flow − whether viewed as deterministically periodic in the early stages or "statistically periodic" (i.e., *cyclo-stationary*) later on − we begin with statistical harmonic analysis tools. These tools are well-suited for investigating the earlier transition stages up to approximately the point of maximum skin friction.

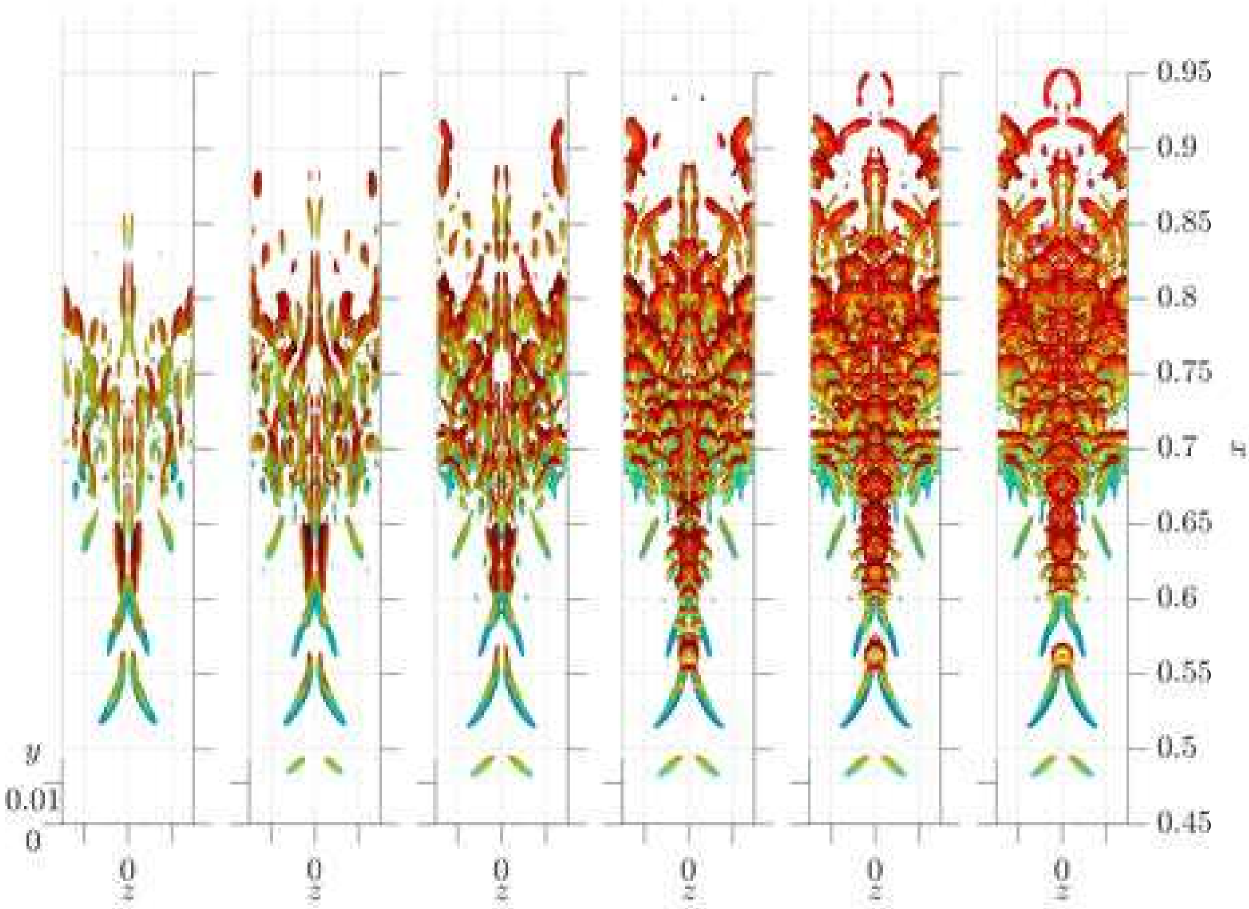

Fig. 3 Superposition of the dominant SPOD modes $\psi^{(1)}_{f_n}$ at harmonic frequencies n in ascending order ($n = 1, 2, 4, 8, 16, 32$ harmonics). Q-criterion isosurfaces colored in the stream-wise velocity ($Q = 10^3$), corresponding to $Re_x = 2.25 - 4.75 \times 10^5$.

The K-type transition, often termed fundamental due to the growth of instabilities caused by the fundamental frequency and its harmonics, has been extensively investigated in the literature using harmonic Fourier analysis methods. However, as this system is a turbulent flow that produces non-periodic statistical data, a naive (long-time) Fourier transform is insufficient, as this kind of estimate of the spectral densities does not converge with increasing data. In order to shed light on the spectral content of this flow and educe the most statistically dominant, convergent, harmonic coherent structures from data that represents this flow at the important frequencies, we apply SPOD to the symmetric and anti-symmetric components $\mathbf{q}_S$ and $\mathbf{q}_A$ individually.

To statistically converge SPOD modes, the best-practice procedure to select the necessary time sampling and spectral estimation parameters for the present K-type DNS is the following: The starting point is the fundamental (angular) excitation frequency $\omega_1 = 55$, which results in a fundamental period of $T_1 = 0.1142$. Since this is a turbulent flow, frequency contents below the lowest fundamental excitation frequency (e.g. subharmonics) could appear and having a sufficient temporal resolution is necessary. Thus we choose to fit eight periods (a convenient power of two) into one N_{FFT} window where we choose a reasonable resolution of $N_{\mathrm{FFT}} = 512$, giving each actuation cycle a resolution of $N_{t,T_1} = 64$ snapshots. This choice results in a physical snapshot sampling time of $\Delta t_{\mathrm{snap}} = 1.785 \times 10^{-3}$. This physical sampling time must be exactly met by an integer multiple of simulation time steps Δt_{DNS}. Using the CFL < 1 condition as constraint, we thus obtain a fixed DNS simulation time step of $\Delta t_{\mathrm{DNS}} = 5.95 \times 10^{-6}$, i.e. we take a snapshot every 300 DNS time steps. The sampling time Δt leads to a sampling frequency of $f_s = 560.22$, thus a Nyquist frequency of $f_{\max} = 280.11$, which has been determined to be sufficient to prevent aliasing. Thereby, the width of one frequency bin Δf, which is also the lowest frequency the SPOD can capture, is then

$$\Delta f = f_{\min} = \frac{1}{N_{\mathrm{FFT}} \Delta t}. \tag{12}$$

Now, to reach statistical convergence of the spectral densities we need a reasonable number of blocks (flow realizations) N_{blk}, where

$$N_{\mathrm{blk}} = \left\lfloor \frac{N_t - N_{\mathrm{ovlp}}}{N_{\mathrm{FFT}} - N_{\mathrm{ovlp}}} \right\rfloor, \tag{13}$$

with an overlap N_{ovlp} between blocks. We use a best-practice 50% overlap and determine with numerical convergence experiments a number of blocks of $N_{\mathrm{blk}} \geqslant 20$ as sufficient. This ultimately leads us to (at least) $N_t = 5376$ DNS snapshots.

Figure 4 provides insights into the distribution of "signal to noise" between the symmetric and anti-symmetric components in the data through the SPOD spectra for $\mathbf{q}_S$ and $\mathbf{q}_A$. In the $\mathbf{q}_S$ spectrum, a dominance by harmonics of the fundamental forcing frequency $f_1 = 8.75$ is evident, with no discernible sub- or ultra-harmonic content. Furthermore, a strong rank decay at all frequency peaks in $\mathbf{q}_S$ indicates the presence of statistically dominant structures at the fundamental frequency and its harmonics. The first SPOD modes capture on average 77% of the space-time energy among the first 8 harmonic peaks and 57% on average for the remaining higher harmonics. Conversely, the $\mathbf{q}_A$ spectrum is essentially flat, showing no distinct peaks and exhibiting very slow rank decay. This noise-like spectrum suggest that there are little to no statistically preferential structures in the anti-symmetric component. Hence, the spectra reveal that the statistically relevant harmonic coherent structures in the transition are all symmetric. While this might seem intuitive given the symmetric periodic actuation, it is worth noting that many fluid flows with clear D1 symmetries exhibit strong anti-symmetry in their modes (e.g., cylinder flow or general bluff body flows). Nevertheless, our harmonic analysis will thus focus on the symmetric part, deferring the exploration of the anti-symmetric content until later.

The dominant coherent structures at a given frequency are represented by the symmetric 1st SPOD modes $\boldsymbol{\psi}^{(1)}_{f_k}$, corresponding to the peaks $f_k = f_n$ of Fig. 4a. We can assemble them into a linear combination at the harmonics $n \in \mathbb{Z}$

$$\sum_n E\left\{\boldsymbol{\psi}^{(1)}_{f_n} a^{(1)}_{f_n}(n_{\mathrm{b}})\right\}_{n_{\mathrm{b}}} e^{(i2\pi f_n t)} + \bar{\mathbf{q}}(\mathbf{x}) \tag{14}$$

with the time-averaged mean flow $\bar{\mathbf{q}}(\mathbf{x})$, block-wise expectation operator $E\left\{\cdot\right\}_{n_{\mathrm{b}}}$ and the 1st block-wise SPOD expansion coefficients $a^{(1)}_{f_n}(n_{\mathrm{b}})$ with $n_{\mathrm{b}} \in [1, N_{\mathrm{blk}}]$, to reconstruct the dominant harmonic content of the entire transition process. Then, we can directly compare the results of various harmonic linear combinations of SPOD modes with those obtained using a harmonic balancing method, as deployed in Rigas et al. [1]. It is worth noting that their study also involves one additional decomposition into a spanwise harmonic basis in z. Specifically, eq. (14) is effectively an upper bound – as these modes are educed “a posteriori” from fully resolved DNS data – and thereby provides the extent to which an “a priori” truncated frequency domain model would be inadequate in capturing the complete transition mechanism at any given level of truncation n. Fig. 3 holistically illustrates the progression of various linear combination levels of SPOD modes at harmonics n with the Q-criterion

$$Q = 1/2(||\boldsymbol{\Omega}||^2 - ||\boldsymbol{S}||^2), \tag{15}$$

the second invariant of the velocity gradient tensor that is comprised of the vorticity tensor $\boldsymbol{\Omega}$ and strain rate tensor $\boldsymbol{S}$. Congruent with results by Rigas et al. [1], indeed only a few SPOD modes are required to accurately reproduce the early transitional, pre-skin-friction-overshoot dynamics. To qualitatively capture hairpin vortices in their early stages, a range of 2-4 SPOD mode harmonics suffice to capture the Λ-vortices, the “legs” of the hairpins. Thereby, various early-stage instability mechanisms including TS, streaks, varicose and sinuous oscillations are well-captured within the 4-harmonic

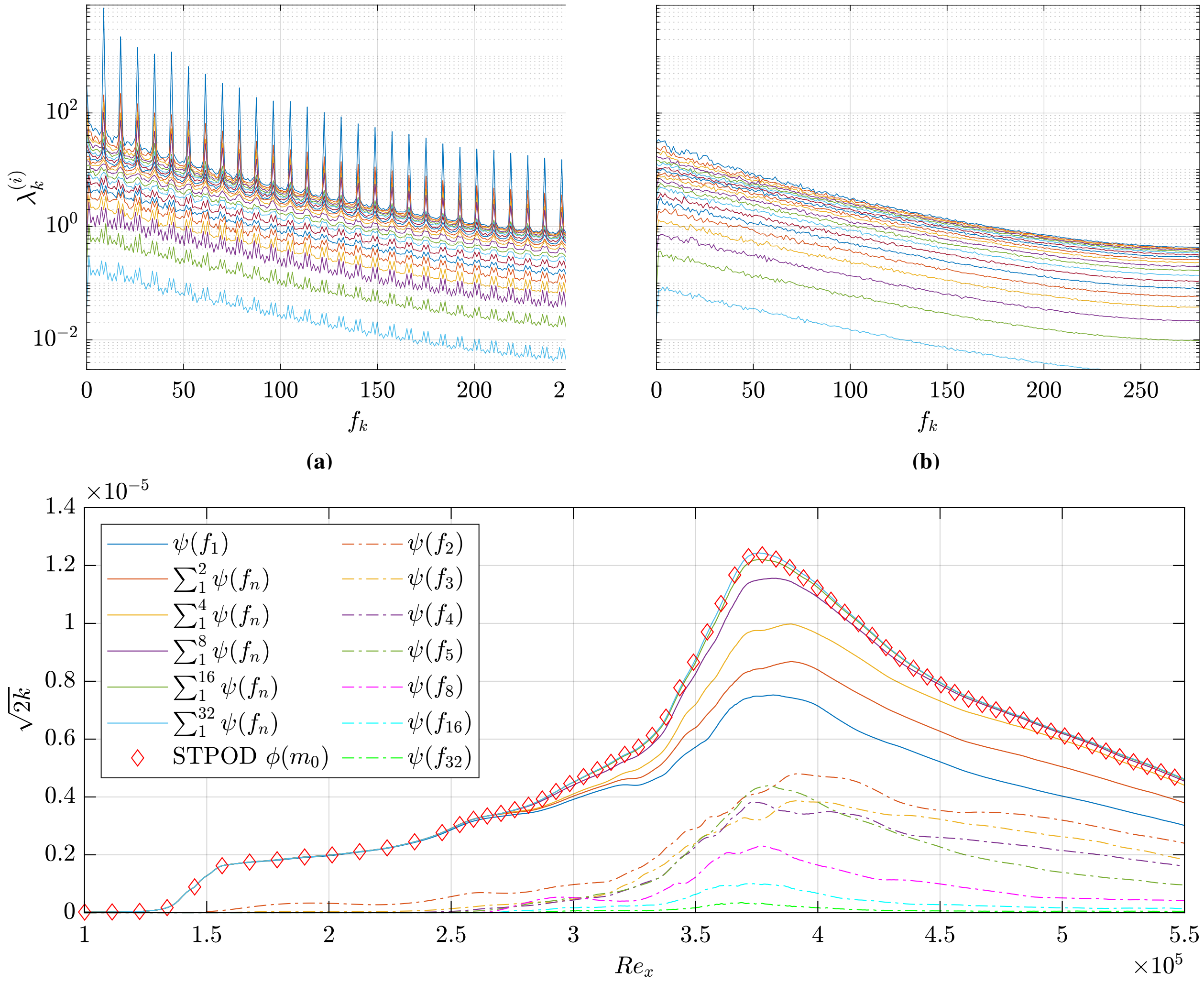

(a) **(b)**

(c)

Fig. 4 SPOD modal energy spectra for a) $\mathbf{q}_S$ and b) $\mathbf{q}_A$ symmetric and anti-symmetric components, respectively, and c) Streamwise energetic development of individual dominant SPOD modes $\psi_{f_n}^{(1)}$ at the harmonic peaks $n \in \mathbb{Z}$ and different orders of their linear combinations.

case, as demonstrated in [1], so we will not detail this further here. However, capturing even a semblance of the initial train of Ω ring-like vortex "heads", occurring approximately between $x = 0.55 - 0.65$ ($Re_x = 2.75 - 3.25 \times 10^5$), already requires *at least* 8 SPOD harmonics. The second more convolved formation of Ω vortices further downstream around $x = 0.65 - 0.75$ appears qualitatively captured within $n = 16$ harmonics. However, observing e.g. the section $x = 0.55 - 0.6$, one notices that adding these higher harmonics also produces higher wavenumber oscillations within space that are not physical but merely a byproduct of the choice of a spatial basis that is harmonic in time. It requires additional harmonics to cancel out the oscillations created by preceding modes. Thus, this flow needs a substantial number of harmonics to construct spatially and temporally *localized*, compact structures via destructive superposition and this is ultimately only fully achieved with the inclusion of all 32 available harmonics. This means that any harmonic balancing method or other reduced-order modeling approach with a harmonic basis must incorporate an equal number of frequencies in its modeling basis to correctly capture the entirety of mechanisms in the transition. Consequently, it raises the question of whether a harmonic Fourier basis, whether in frequency or wavenumber space, is in fact the most suitable choice for simulating or analyzing flow problems characterized by highly localized coherent structures

Nevertheless, we want to dissect and understand the energetic contribution of individual components. For that purpose, we measure the streamwise energetic progression in form of the RMS of the total fluctuation vector as energy metric, given by

$$\sqrt{2\mathrm{k}} = \sqrt{E\{u'^2 + v'^2 + w'^2\}_{y,z,t}} \tag{16}$$

averaged in time, spanwise and/or wall-normal directions. This quantifies the average turbulent kinetic energy square-root of a flow component in any given y-z-plane along the streamwise direction x. The choice of square root is intentional, to be in the units of velocity and to not skew the view towards large or away from small values. Fig. 4c details that streamwise energetic development for the optimal modes $\boldsymbol{\psi}_{f_n}^{(1)}$ for both the individual frequency components as well as for different levels of modal superposition. Congruent with Fig. 2a, it reveals that the early flow development ($Re_x \leqslant 2.5 \times 10^5$) is energetically dominated by the fundamental SPOD mode at f_1 (fundamental TS instability) as it carries almost of the oscillatory energy until then, with only the harmonic f_2 trailing at low energy levels beneath it. The higher harmonics only begin to take off beyond $Re_x \geqslant 2.5 \times 10^5$, congruent with the departure of skin-friction in Fig. 2b from the laminar solution and the appearance of Λ-vortices and all of them peak around the C_f maximum. Observationally, there is a notable variability in the peaking behavior among different frequency components, as some exhibit earlier peaks while others peak later, each with varying maxima. For instance, when f_5 peaks, it demonstrates locally higher energy compared to any other components – also evident in Fig. 4a, where $\lambda_{f_5}^{(1)}$ displays greater energy than its adjacent harmonics. This variation in peaking behavior motivates an exploration of different triadic interactions and energy transfers between triad combinations. Methods like Bispectral Mode Decomposition (BMD) [21], as employed by Nekkanti et al. [22] in the study of forced and unforced jet flows, could offer valuable insights into these dynamics.

More significantly, Fig. 4c highlights the convergence of the harmonic superposition of optimal SPOD modes towards another notable statistical quantity. Specifically, the superposition of 32 SPOD modes aligns with the phase mean, which itself represents the fundamental symmetric STPOD mode $\boldsymbol{\phi}_0$ (equivalence will be shown in IV.B). These quantities all represent the statistically prototypical, periodic transition scenario. Thus, one statistical benchmark to compare a harmonic modal decomposition to is the periodic phase mean that encompasses the fundamental frequency and all its harmonics. To develop a notion for "statistically periodic", we briefly introduce the concepts of *cyclo-stationarity* and phase-averaging: A process $\mathbf{q}(\mathbf{x}, t)$ is cyclostationary [23] if its mean $E\{\mathbf{q}(\mathbf{x}, t)\}$ and cross-correlation $\boldsymbol{C}(\mathbf{x}, \mathbf{x}, t, \tau)$ functions (with some time-delay τ) are periodic with fundamental period T_1, expressed as

$$\begin{aligned} E\{\mathbf{q}(\mathbf{x}, t)\} &= E\{\mathbf{q}(\mathbf{x}, t + T_1)\}, \\ \boldsymbol{C}(\mathbf{x}, \mathbf{x}, t, \tau) &= \boldsymbol{C}(\mathbf{x}, \mathbf{x}, t + T_1, \tau). \end{aligned}$$

If $\mathbf{q}(\mathbf{x}, t)$ contains a deterministic periodic component at cycle frequency nf_1 (where $f_1 = 1/T_1$ and $n \in \mathbb{Z}$, i.e. an integer multiple of the cycle frequency), it exhibits first-order and second-order (& higher-order) cyclo-stationarity at nf_1. The second-order component $\mathbf{q}''(\mathbf{x}, t)$ is defined as

$$\mathbf{q}''(\mathbf{x}, t) \equiv \mathbf{q}(\mathbf{x}, t) - E\{\mathbf{q}(\mathbf{x}, t)\}, \tag{17}$$

which separates the deterministic first-order (tonal) component from the stochastic second-order (turbulent) component.

Thus, for data that is phase-locked, the cycle-averaging operator is given by

$$\tilde{\mathbf{q}}(\mathbf{x},t) = \lim_{N_{T_1}\to\infty} \frac{1}{N_{T_1}} \sum_{m=0}^{N_{T_1}} \mathbf{q}(\mathbf{x}, t + mT_1), \tag{18}$$

to obtain $\tilde{\mathbf{q}}(\mathbf{x},t)$ the periodic phase mean, where N_{T_1} is the number of fundamental periods contained in the data. Optionally, one can use one more decomposition into the stationary long-time mean $\bar{\mathbf{q}}(\mathbf{x})$, such as in the triple decomposition by Hussain and Reynolds [24] or utilized by Bake et al. [5], which results in $\mathbf{q}(\mathbf{x},t) = \bar{\mathbf{q}}(\mathbf{x}) + \tilde{\mathbf{q}}(\mathbf{x},t) + \mathbf{q}''(\mathbf{x},t)$.

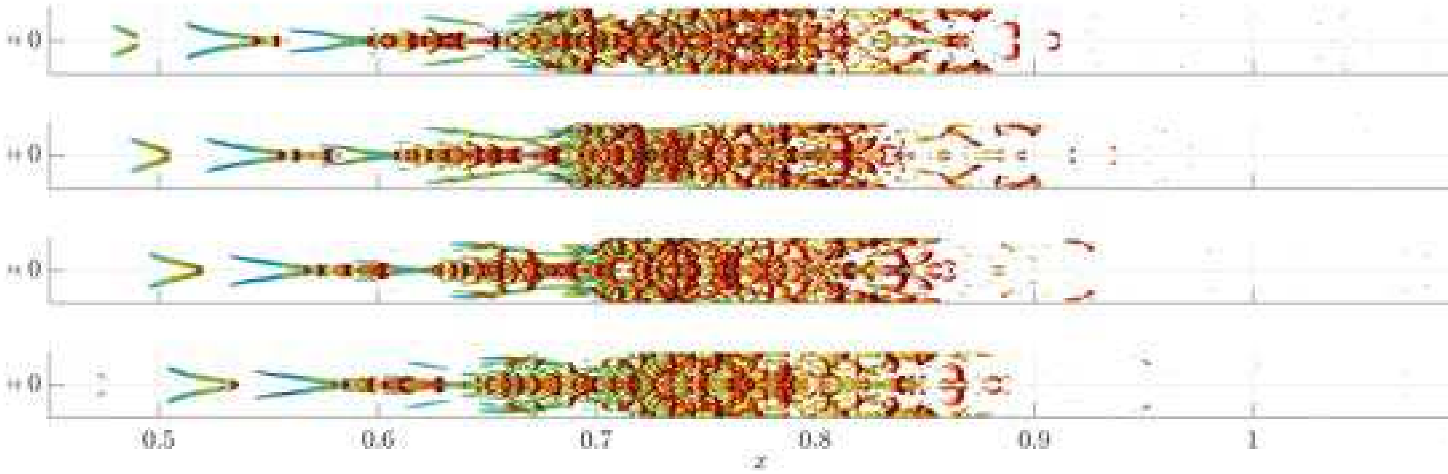

Fig. 5 Harmonic coherent structure of the transition at four different phases $0T_1$, $0.25T_1$, $0.5T_1$, $0.75T_1$ within the fundamental period T_1 – identified by phase mean (fundamental STPOD mode ϕ_0) and the order $n = 32$ harmonic superposition of dominant SPOD modes. Q-criterion visualization colored in streamwise velocity ($Q = 10^3$), corresponding to $Re_x = 2.25 - 5 \times 10^5$.

We note that, as it is a priori unknown to what degree a given turbulence dataset is dominated by harmonic statistics, we apply SPOD here that is generally optimal for statistically stationary flows. This is justifiable, as the present flow statistics evolve through periodic, cyclo-stationary and finally statistically stationary (fully turbulent) regimes. On the other hand, with the now a posteriori knowledge on the coherent harmonic content of the flow, one can opt to analyze to what degree this modulates the cyclo-stationary second-order statistics $\mathbf{q}''(\mathbf{x},t)$ within the frequency domain, thus, apply a more optimal spectral modal decomposition method that is specifically geared towards the statistics that are centered around a periodic phase-mean, see Heidt and Colonius [25]. However, this was not the target of the present harmonic de-/reconstruction study here, as we are interested in the spectral energy content, i.e., the structures and energies contained in each frequency component in the classical Fourier sense.

Still, with the concept of cyclo-stationarity and the phase mean established, $\tilde{\mathbf{q}}(\mathbf{x},t)$ will now be taken as new reference point for the next analysis section, i.e. the periodic phase mean will now be assumed as given and subtracted from the data to focus on the generally non-harmonic, cyclo-stationary second-order statistics $\mathbf{q}''(\mathbf{x},t)$.

B. Breaking Periodicity and Symmetry − Path to Developed Turbulence

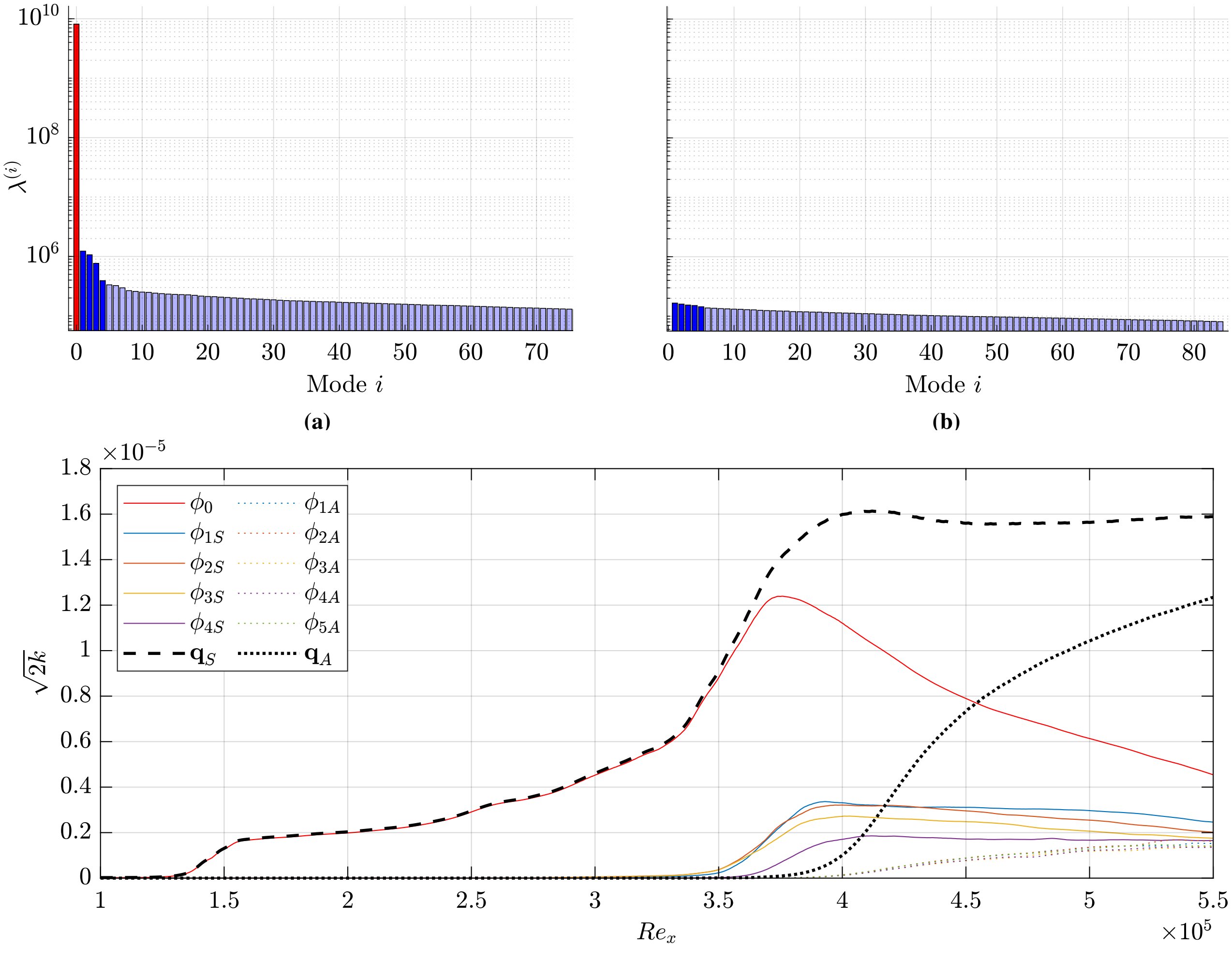

(a) **(b)**

(c)

Fig. 6 STPOD modal energy spectra for a) $\mathbf{q}_S$ and b) $\mathbf{q}_A$ symmetric and anti-symmetric components respectively and c) streamwise energetic development metrics of individual symmetric and anti-symmetric STPOD modes, enveloped by streamwise energetic development of the total $\mathbf{q}_S$ and $\mathbf{q}_A$ components.

In this concluding analysis section, we move beyond the C_f maximum into the turbulent regime, necessitating a departure from the assumptions of periodicity and symmetry. The time dynamics here evolve from periodic to quasi-periodic, eventually breaking periodicity and culminating in chaotic/turbulent behavior. As symmetry is broken following the breakdown of periodicity, the applicability of harmonic analysis diminishes. Consequently, the need arises for modal decomposition methods capable of identifying general space-time modes with non-periodic time trajectories. In this context, STPOD emerges as a fitting choice for capturing the evolving dynamics in the later transitional regime.

In the context of this cyclo-stationary flow, STPOD amounts to a weighted singular value decomposition of the space-time Hankel matrix, whose columns are each assembled by N_{t,T_1} flow snapshots within a given period. Thus, the columns each represent different flow trajectory realizations from a given actuation cycle. Hence, the dominant space-time mode naturally converges to the phase mean, verifiable by averaging the columns of the Hankel matrix. This allows the formation of the fundamental STPOD mode through phase-averaging, enabling its subtraction from the Hankel matrix and computation of STPOD without it. This aligns with statistics practices, as it is well-known that for statistically stationary data with a non-subtracted long time mean that the mean is naturally recovered as first mode. Analogously, for our cyclo-stationary data the phase mean is naturally recovered as first mode and can thus be subtracted to center the data. We can subsequently add it back as the 0th mode with constant expansion coefficients to describe a (low-rank) reconstruction of the full flow field, i.e.

$$\mathbf{q}(\mathbf{x},t) = \mathbf{q}''(\mathbf{x},t) + \tilde{\mathbf{q}}(\mathbf{x},t) = \sum_m \boldsymbol{\phi}_m(\mathbf{x},t)a_m(j) + \tilde{\mathbf{q}}(\mathbf{x},t) \equiv \sum_m \boldsymbol{\phi}_m(\mathbf{x},t)a_m(j) + \boldsymbol{\phi}_0(\mathbf{x},t), \tag{19}$$

where $a_m(j)$ denotes the realization-dependent expansion coefficients with $j \in [1, N_{T_1}]$. This aligns with common convention in reduced order modeling [26, 27]. Irrespectively, the phase mean (whether identified as the 1st mode in the no-subtraction approach or via phase-averaging) should be regarded as the fundamental space-time mode because it has by far the highest space-time energy in the norm of eq. 4 (see Fig. 6a, red bar) and is orthogonal to the remaining modes within numerical precision. For the purpose of this paper, we therefore denote the phase mean as the fundamental 0th STPOD mode $\boldsymbol{\phi}_0$, distinguishing it from the 1st non-fundamental STPOD mode $\boldsymbol{\phi}_{1S}$ (which becomes the 2nd mode in the no-subtraction approach) identified as a result of variance within the cyclo-stationary turbulence data.

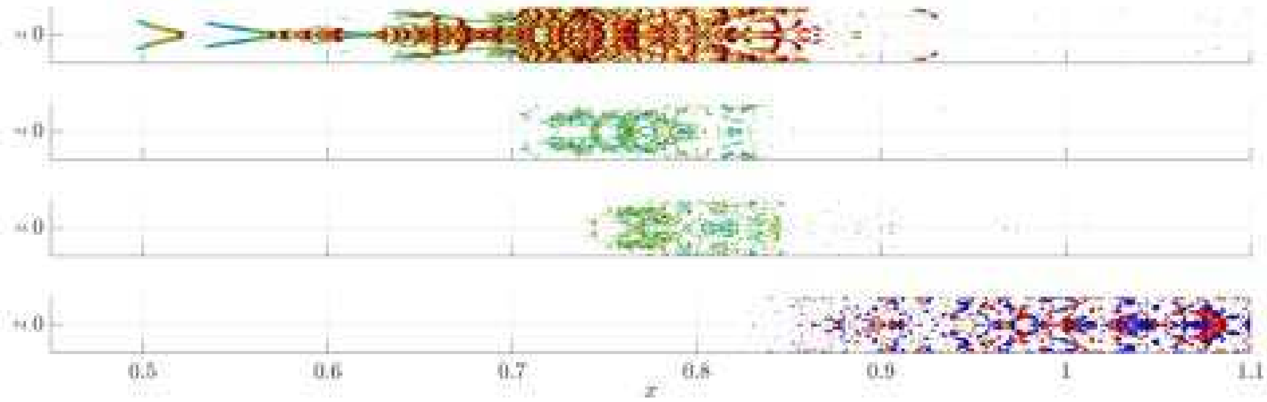

Fig. 7 Path to chaos – various STPOD modes at the same phase: 1) to 3) fundamental mode $\boldsymbol{\phi}_0$ and non-fundamental symmetric modes $\boldsymbol{\phi}_{1S}$ and $\boldsymbol{\phi}_{4S}$, Q-criterion isosurfaces ($Q = 1 \times 10^3, 1 \times 10^3, 0.3 \times 10^3$ respectively) colored in their own streamwise velocity; 4) w velocity component of the linear combination of first 5 anti-symmetric STPOD modes, $w = \pm 0.02$ isosurfaces (red:+, blue:−), all corresponding to $Re_x = 2.25 - 5.5 \times 10^5$.

As Fig. 5 shows, the fundamental symmetric STPOD mode $\boldsymbol{\phi}_0$, with its Q-criterion vanishing beyond roughly $x > 0.9$ ($Re_x > 4.5 \times 10^5$), is a coherent structure with compact spatial support representing the prototypical transition scenario. Remarkably, Fig. 6c also reveals that the entire flow up to just before $Re_x = 3.5 \times 10^5$ is energetically entirely described by the periodic dynamics of the fundamental STPOD mode, no other flow component exhibits any energy up to that point. Here it is crucial to re-emphasize that STPOD (unlike SPOD or other harmonic analysis methods) does not identify periodic structures by construction or by default – it does not impose any sort of assumption on the time-dynamics of the to-be-identified modes. STPOD in general is applicable to even transient events [28], though, as we define the finite time window as one actuation period, we can expect to recover cyclostationary statistics (periodic dynamics) within certain modes that correspond to the early and transitional region, *if* they in fact have periodic trajectories in the first place. On the contrary, we can expect statistically stationary statistics (non-periodic dynamics) for modes corresponding to the later turbulent regime.

As detailed above, there is no doubt that $\boldsymbol{\phi}_0$ describes a good amount of the dynamics in the boundary layer transition process but only for the early and transitional regimes where the flow is periodic and cyclo-stationary. $\boldsymbol{\phi}_0$ becomes insufficient in representing the flow and describing its dynamics in the later regimes, further downstream beyond the C_f maximum, where periodicity is broken. The first three non-fundamental symmetric STPOD modes $\boldsymbol{\phi}_{1S}$, $\boldsymbol{\phi}_{2S}$ and $\boldsymbol{\phi}_{3S}$ slowly arise around $Re_x = 3.4 \times 10^5$. Statistically, they represent the first signs of variance from the purely periodic phase mean. Upon inspection of their dynamics, they themselves are also periodic, i.e.

$$\boldsymbol{\phi}_{mS}(\mathbf{x}, t \to T_1) = \boldsymbol{\phi}_{mS}(\mathbf{x}, t \to 0), \quad m = \{1, 2, 3\}. \tag{20}$$

Dynamically, this means that as the flow, that initially starts out as deterministic with no variance and fully described by the periodic $\boldsymbol{\phi}_0$, progresses further downstream the first few bifurcations occur: Here $\boldsymbol{\phi}_{1S}$, $\boldsymbol{\phi}_{2S}$ and $\boldsymbol{\phi}_{3S}$ perturb the fluid state from the purely periodic limit cycle of the $\boldsymbol{\phi}_0$ mode onto their own alternate limit cycles given by their own dynamics. In the sum this creates a *quasi-periodic* trajectory in the local region around $Re_x = 3.4 - 3.7 \times 10^5$, in which the state switches unstably between the different components' limit cycles. Mathematically, this is given by

$$\mathbf{q}_{\Sigma_0^3 S}(\mathbf{x}, t) = \boldsymbol{\phi}_0(\mathbf{x}, t) + \boldsymbol{\phi}_{1S}(\mathbf{x}, t) a_{1S}(j) + \boldsymbol{\phi}_{2S}(\mathbf{x}, t) a_{2S}(j) + \boldsymbol{\phi}_{3S}(\mathbf{x}, t) a_{3S}(j), \tag{21}$$

where the subscript denotes the linear combination of the first 3 symmetric modes and the fundamental. The *timing* and *amplitude* of the switching is explicitly given by the respective expansion coefficients $a_{1S}(j)$, $a_{2S}(j)$, $a_{3S}(j)$ that vary over the realizations j and thereby modulate the locally quasi-periodic dynamics.

The flow up to this point has been well-described by the fundamental and first three STPOD modes, i.e. $\mathbf{q}(\mathbf{x}, t) \approx \mathbf{q}_{\Sigma_0^3 S}(\mathbf{x}, t)$ up to $Re_x \leqslant 3.7$. It is around this location where the fourth non-fundamental symmetric STPOD mode $\boldsymbol{\phi}_{4S}$ arises – Fig. 7 shows its slightly further downstream spatial support compared to $\boldsymbol{\phi}_{1S}$. Most notably, $\boldsymbol{\phi}_{4S}$ is characteristically different: It is the first mode within the symmetric STPOD spectrum in Fig. 6a to break the pattern of periodicity. Upon inspection of its dynamics, there is a clear discontinuous jump in its trajectory from its last ($t \to T_1$) to its first frame ($t \to 0$), that is

$$\boldsymbol{\phi}_{4S}(\mathbf{x}, t \to T_1) \neq \boldsymbol{\phi}_{4S}(\mathbf{x}, t \to 0). \tag{22}$$

All symmetric modes that follow become increasingly non-periodic and increasingly further downstream. Dynamically, this signals the onset of *chaos* starting from this point. The thus far quasi-periodic state trajectory departs here from its limit cycle(s) and does not return anymore after one or multiple periods.

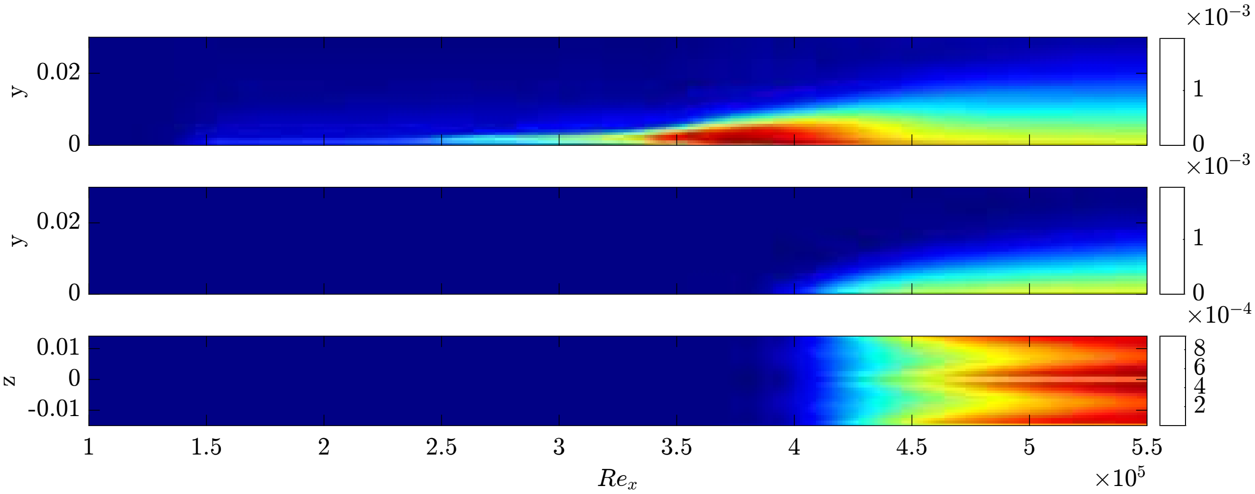

Fig. 8 Time-averaged $\sqrt{2k}$ energy metrics of the $\mathbf{q}_S$ and $\mathbf{q}_A$ components as various integrated spatial maps. Top: $\mathbf{q}_S$ integrated in z. Middle: $\mathbf{q}_A$ integrated in z (same color scale as top). Bottom: $\mathbf{q}_A$ integrated in y.

It is remarkable that so far, the entire flow has been completely symmetric and is hence entirely described by the symmetry component $\mathbf{q}_S$. The first signs of the symmetry being broken occurs around $Re_x \geqslant 3.8 \times 10^5$: As Fig. 6c shows, the $\sqrt{2\text{k}}$ energy metric of the total anti-symmetric component $\mathbf{q}_A$ starts to lift off and increase as the flow progresses downstream towards more developed turbulence. The individual anti-symmetric STPOD modes all start to arise slowly, with no apparent preference one over another and none of the anti-symmetric modes have periodic dynamics, as they are all located in the turbulent regime. This should not surprise, as already shown in the SPOD spectra in Fig. 4b and confirmed again in the STPOD spectra of Fig. 6b, the anti-symmetric component $\mathbf{q}_S$ exhibits a noise-like, flat mode spectrum. Hence, we do not attempt to explain the spatial structure of the individual modes. The fact that again there are no statistically dominant structures hints at the possibility that the symmetry breaking here could be non-modal, however more investigation is needed.

A notable mechanism observed in the region that immediately follows ($Re_x \geqslant 4.1 \times 10^5$) is the slight dip followed by the apparent plateauing in the energy metric of the total symmetric component $\mathbf{q}_S$, suggesting a rapid transfer of energy from the symmetric component to the anti-symmetric component. The upper and middle plots in Fig. 8 visualize this, where the z-integrated $\sqrt{2k}$ energy metric for $\mathbf{q}_S$ appears to cool off rapidly (after peaking in the C_f-overshoot zone), while simultaneously the energy metric for $\mathbf{q}_A$ increases. Fig. 7 further supports this by depicting the streamwise spatial support in form of the Q-criterion. The coherent vortices of the fundamental mode $\boldsymbol{\phi}_0$ (and $\boldsymbol{\phi}_{1S}$, $\boldsymbol{\phi}_{4S}$) start breaking down rapidly, i.e. their Q goes into a more strain dominant than vorticity dominant state $||\boldsymbol{\Omega}||^2 < 2Q + ||\boldsymbol{S}||^2$. Thus, the symmetric modes lose coherence as the anti-symmetric modes arise and gain in fluctuation and energy. Future work on a cross-BMD between the $\mathbf{q}_S$ and $\mathbf{q}_A$ components may shed light on the exact interactions that cause this phenomenon.

Finally, as it is not useful to look at individual anti-symmetric modes (no statistically dominant structures) we can attempt to find spatial patterns in the time-averaged $\sqrt{2\mathrm{k}}$ energy metric of $\mathbf{q}_A$ as a whole. The bottom plot in Fig. 8 depicts the y-integrated $\sqrt{2\mathrm{k}}$ as spatial distribution in the x-z-plane and shows that the anti-symmetry appears to start and have highest energy around the mid plane and periodic boundaries of the domain. Revisiting eq. (2), we note that by definition

$$\mathbf{q}_A(x, y, z = 0) = \begin{bmatrix} 0 \\ 0 \\ w(x, y, z = 0) \end{bmatrix}, \tag{23}$$

so if there is any non-zero w velocity (spanwise flow) on the midplane $z = 0$, the flow is anti-symmetric. Similarly, if there is spanwise flow through the periodic boundaries that is also by definition anti-symmetric. Furthermore, the u and v velocities of the anti-symmetry component on these planes are 0 by construction. Hence a non-zero fluctuation energy on any of those planes signals the existence of a z velocity that is breaking the symmetry. Thus, Fig. 8 demonstrates that, as the flow progresses downstream, the symmetry breaking statistically occurs through these planes first. For an instantaneous visualization, the bottom plot of Fig. 7 shows isosurfaces of w velocity fluctuations of an exemplary superposition of the first 5 anti-symmetric STPOD modes $\mathbf{q}_{\Sigma_1^5 A}(\mathbf{x}, t)$. Observing any continuous contour, whether blue or red, that crosses the $z = 0$ plane or connects the spanwise periodic $z = \pm 0.015$ boundaries means that the symmetry is being broken at a given point.

V. Conclusion

Our analysis of K-type boundary layer transition uses modal decomposition techniques to unveil the underlying statistics and dynamics as the flow progresses from periodic excitation to fully developed turbulence. Harmonic analysis using Spectral Proper Orthogonal Decomposition (SPOD) reveals the dominant coherent structures in the early and transitional regimes. Our investigation shows that the early stages of transition are predominantly characterized by periodic (cyclo-stationary), symmetric structures, as evidenced by the dominance of the fundamental SPOD mode and its harmonics. This allows for the reconstruction of the dominant coherent transition mechanisms through a linear combination of these modes. However, as the flow advances beyond the critical point marked by the skin friction coefficient (C_f) maximum, periodicity and symmetry begin to break down. To capture the evolving dynamics beyond the periodic phase, we use Space-Time Proper Orthogonal Decomposition (STPOD), to identify non-periodic spatio-temporal structures. The fundamental STPOD mode $\boldsymbol{\phi}_0$ emerges as a coherent structure describing the periodic cyclo-stationary state, offering an insightful perspective into the early transitional dynamics. As the flow progresses further downstream, the emergence of non-fundamental symmetric STPOD modes ($\boldsymbol{\phi}_{1S}$, $\boldsymbol{\phi}_{2S}$, $\boldsymbol{\phi}_{3S}$) signifies the initiation of quasi-periodic behavior. This quasi-periodicity eventually gives way to chaos, marked by the appearance of the fourth symmetric non-periodic STPOD mode ($\boldsymbol{\phi}_{4S}$) and subsequent non-periodic modes. Simultaneously, the anti-symmetric component gains prominence, indicating the breakdown of symmetry. We make observations about the energy transfer from the symmetric to the anti-symmetric component, evident in the energy metric profiles. The breakdown of coherent vortices and the appearance of anti-symmetry mark the transition to fully developed turbulence. Symmetry breaking is identified first around the midplane and periodic planes, suggesting a spatially selective evolution of anti-symmetry. In conclusion, our study offers a further understanding of the intricate dynamics in the boundary layer transition, emphasizing the interplay between periodicity, non-periodicity and symmetry on the path to fully developed boundary layer turbulence.

Acknowledgments

We acknowledge the NSF for funding this boundary layer transition project under the grant CBET 2046311.

References

[1] Rigas, G., Sipp, D., and Colonius, T., "Nonlinear input/output analysis: application to boundary layer transition," *Journal of Fluid Mechanics*, Vol. 911, 2021.

[2] Rist, U., and Fasel, H., "Direct numerical simulation of controlled transition in a flat-plate boundary layer," *Journal of Fluid Mechanics*, Vol. 298, 1995, pp. 211–248.

[3] Kachanov, Y. S., Kozlov, V., Levchenko, V. Y., and Ramazanov, M., "On nature of K-breakdown of a laminar boundary layer. New experimental data," *Laminar-Turbulent Transition: Symposium, Novosibirsk, USSR July 9–13, 1984*, Springer, 1985, pp. 61–73.

[4] Kachanov, Y. S., and Levchenko, V. Y., "The resonant interaction of disturbances at laminar-turbulent transition in a boundary layer," *Journal of Fluid Mechanics*, Vol. 138, 1984, pp. 209–247.

[5] Bake, S., Meyer, D., and Rist, U., "Turbulence mechanism in Klebanoff transition: a quantitative comparison of experiment and direct numerical simulation," *Journal of Fluid Mechanics*, Vol. 459, 2002, pp. 217–243.

[6] Sayadi, T., Hamman, C. W., and Moin, P., "Direct numerical simulation of complete H-type and K-type transitions with implications for the dynamics of turbulent boundary layers," *Journal of Fluid Mechanics*, Vol. 724, 2013, pp. 480–509.

[7] Sirovich, L., "Turbulence and the dynamics of coherent structures. II. Symmetries and transformations," *Quarterly of Applied mathematics*, Vol. 45, No. 3, 1987, pp. 573–582.

[8] Lumley, J. L., *Stochastic Tools in Turbulence*, 1st ed., Academic Press, New York, 1970.

[9] Schmidt, O. T., and Schmid, P. J., "A conditional space–time POD formalism for intermittent and rare events: example of acoustic bursts in turbulent jets," *Journal of Fluid Mechanics*, Vol. 867, 2019, p. R2.

[10] Frame, P., and Towne, A., "Space-time POD and the Hankel matrix," *arXiv preprint arXiv:2206.08995*, 2022.

[11] Sirovich, L., “Turbulence and the dynamics of coherent structures. I. Coherent structures,” *Quarterly of applied mathematics*, Vol. 45, No. 3, 1987, pp. 561–571.

[12] Aubry, N., “On the hidden beauty of the proper orthogonal decomposition,” *Theoretical and Computational Fluid Dynamics*, Vol. 2, No. 5-6, 1991, pp. 339–352.

[13] Towne, A., Cavalieri, A. V. G., Jordan, P., Colonius, T., Schmidt, O., Jaunet, V., and Brès, G. A., “Acoustic resonance in the potential core of subsonic jets,” *Journal of Fluid Mechanics*, Vol. 825, 2017, pp. 1113–1152.

[14] Towne, A., Schmidt, O. T., and Colonius, T., “Spectral proper orthogonal decomposition and its relationship to dynamic mode decomposition and resolvent analysis,” *Journal of Fluid Mechanics*, Vol. 847, 2018, pp. 821–867.

[15] Welch, P., “The use of fast Fourier transform for the estimation of power spectra: a method based on time averaging over short, modified periodograms,” *IEEE Transactions on audio and electroacoustics*, Vol. 15, No. 2, 1967, pp. 70–73.

[16] Fasel, H. F., Rist, U., and Konzelmann, U., “Numerical investigation of the three-dimensional development in boundary-layer transition,” *AIAA journal*, Vol. 28, No. 1, 1990, pp. 29–37.

[17] Brès, G. A., Ham, F. E., Nichols, J. W., and Lele, S. K., “Unstructured Large-Eddy Simulations of Supersonic Jets,” *AIAA Journal*, Vol. 55, No. 4, 2017, pp. 1164–1184.

[18] White, F. M., *Viscous fluid flow*, Vol. 3, McGraw-Hill New York, 2006.

[19] Wu, X., and Moin, P., “Direct numerical simulation of turbulence in a nominally zero-pressure-gradient flat-plate boundary layer,” *Journal of Fluid Mechanics*, Vol. 630, 2009, pp. 5–41.

[20] Wu, X., and Moin, P., “Transitional and turbulent boundary layer with heat transfer,” *Physics of Fluids*, Vol. 22, No. 8, 2010.

[21] Schmidt, O. T., “Bispectral mode decomposition of nonlinear flows,” *Nonlinear Dynamics*, Vol. 102, 2020, pp. 2479–2501.

[22] Nekkanti, A., Maia, I., Jordan, P., Heidt, L., Colonius, T., and Schmidt, O. T., “Triadic nonlinear interactions and acoustics of forced versus unforced turbulent jets,” *Twelveth International Symposium on Turbulence and Shear Flow Phenomena (TSFP12)*, 2022, pp. 19–22.

[23] Gardner, W. A., Napolitano, A., and Paura, L., “Cyclostationarity: Half a century of research,” *Signal processing*, Vol. 86, No. 4, 2006, pp. 639–697.

[24] Hussain, A. K. M. F., and Reynolds, W. C., “The mechanics of an organized wave in turbulent shear flow,” *Journal of Fluid Mechanics*, Vol. 41, No. 2, 1970, pp. 241–258.

[25] Heidt, L., and Colonius, T., “Spectral proper orthogonal decomposition of harmonically forced turbulent flows,” *arXiv preprint arXiv:2305.05628*, 2023.

[26] Noack, B. R., Morzynski, M., and Tadmor, G., *Reduced-order modelling for flow control*, Vol. 528, Springer Science & Business Media, 2011.

[27] Östh, J., Noack, B. R., Krajnović, S., Barros, D., and Borée, J., “On the need for a nonlinear subscale turbulence term in POD models as exemplified for a high-Reynolds-number flow over an Ahmed body,” *Journal of Fluid Mechanics*, Vol. 747, 2014, pp. 518–544.

[28] Hack, M. P., and Schmidt, O. T., “Extreme events in wall turbulence,” *Journal of Fluid Mechanics*, Vol. 907, 2021, p. A9.